

Low-Threshold Chirality-Enabled Silicon Photonic Diode

Jiewen Li, Ke Li, Wanxin Li, Jinzhao Wang, Yong Yao, Yunxu Sun, Yi Zou,* Jiawei Wang,* Feng He, Jianan Duan, Yongkang Dong, and Xiaochuan Xu*

Optical nonlinearity offers a promising pathway for advancing passive silicon photonic diodes and enabling precise control of on-chip light flow. However, the realization of nonlinearity-based photonic diodes often requires high-power excitation, a common constraint in conventional nonlinear devices. In this study, a passive silicon photonic diode based on a nonlinear chiral microring resonator is proposed. The chiral property is introduced by perturbing the evanescent field with two nanocylinders, which minimizes the additional loss compared to other approaches for initiating chirality. This method significantly reduces the mode volume without compromising the quality (Q) factor, resulting in the experimental demonstration of a $5\text{-}\mu\text{m}$ radius chiral microring with Q factor ≈ 68155 . Consequently, the proposed photonic diode achieves an exceptionally low threshold power of P_{th} ≈ -7.83 dBm. The diode maintains low-threshold nonreciprocal behavior during thermal tuning, facilitating an extended operational bandwidth. This work provides a practical solution for the large-scale integration of passive photonic diodes within silicon photonic circuits.

1. Introduction

Nonreciprocal devices, which display distinct transmission efficiencies when interchanging the source and observation points, are essential building blocks for optical systems.^[1–6] The conventional approach to attain nonreciprocity relies on the magneto-optic (MO) effect.^[6,7] Although MO-based nonreciprocal optical devices are widely used in free-space and fiber-optic systems,^[8]

their implementation in integrated silicon photonic circuits remains challenging because of the bulky magnet and material incompatibility.^[9] A few magnetic-free approaches, such as spatiotemporal modulation,^[4] optomechanics,^[10] and optical nonlinearity,^[3,5,11] have been extensively investigated to circumvent the barriers. Because of the bias-free operation^[3] and the inherent presence of optical nonlinearity in silicon,^[8] the nonlinearity-based approach has emerged as a promising avenue for implementing nonreciprocal optical devices in integrated silicon photonic circuits.^[8,12–19] Despite the constraints imposed by dynamic reciprocity,^[20] nonlinearity-based nonreciprocal devices can function as photonic diodes when simultaneous multiport excitation is not expected.^[8,13,18] These photonic diodes are commonly implemented using a

Fano microresonator.^[8,11–14,18,21] The asymmetric permittivity profile of the Fano microresonator in the nonlinear regime is utilized to construct a passive photonic diode.^[11] However, the diodes based on nonlinear Fano microresonators are typically limited by the intrinsic trade-off between spectral bandwidth and insertion loss.^[3] Although the trade-off can be overcome by employing cascading multiresonators,^[15,29] the resonances in such multiresonator systems must satisfy stringent phase-matching conditions.

Recently, chiral microresonators have attracted significant attention due to their unprecedented ability to control the flow of light on a chip,^[22–24] which fertilizes a plethora of fascinating phenomena, including unidirectional emission,^[25] ultrahigh enhanced sensing,^[26,27] electromagnetically induced transparency,^[28] reconfigurable mode chirality,^[29] coherent perfect absorption,^[30] magnetic-free nonreciprocity,^[31–33] and chiral absorption.^[34] In the linear regime, the chiral microresonator exhibits symmetric transmission as predicted by the Lorentz reciprocity theorem.^[1] When the chiral microresonator is steered into the nonlinear regime, a nonreciprocal band emerges.^[31–33] Because nonreciprocal spectral bandwidth and insertion loss are independent in the nonlinear regime, chiral microresonators hold significant potential for breaking the trade-off in nonlinearity-based photonic diodes.^[33] Although nonreciprocity has been demonstrated in nonlinear chiral microresonators made of silica^[33] and silicon oxynitride,^[31,32] the implementation in silicon photonics is crippled by the high excitation power threshold constrained by the limited Q

J. Li, K. Li, W. Li, J. Wang, Y. Yao, Y. Sun, J. Wang, F. He, J. Duan, Y. Dong, X. Xu

National Key Laboratory of Laser Spatial Information
Guangdong Provincial Key Laboratory of Integrated Photonic-Electronic Chip

Guangdong Provincial Key Laboratory of Aerospace Communication and Networking Technology

Harbin Institute of Technology

Xili University Town

Harbin Institute of Technology campus

Shenzhen, Guangdong 518055, China

E-mail: wangjw7@hit.edu.cn; xuxiaochuan@hit.edu.cn

Y. Zou

School of Information Science and Technology

ShanghaiTech University

Shanghai 201210, China

E-mail: zouyi@shanghaitech.edu.cn

X. Xu

Pengcheng Laboratory

Shenzhen, Guangdong 518055, China

DOI: 10.1002/lpor.202402078

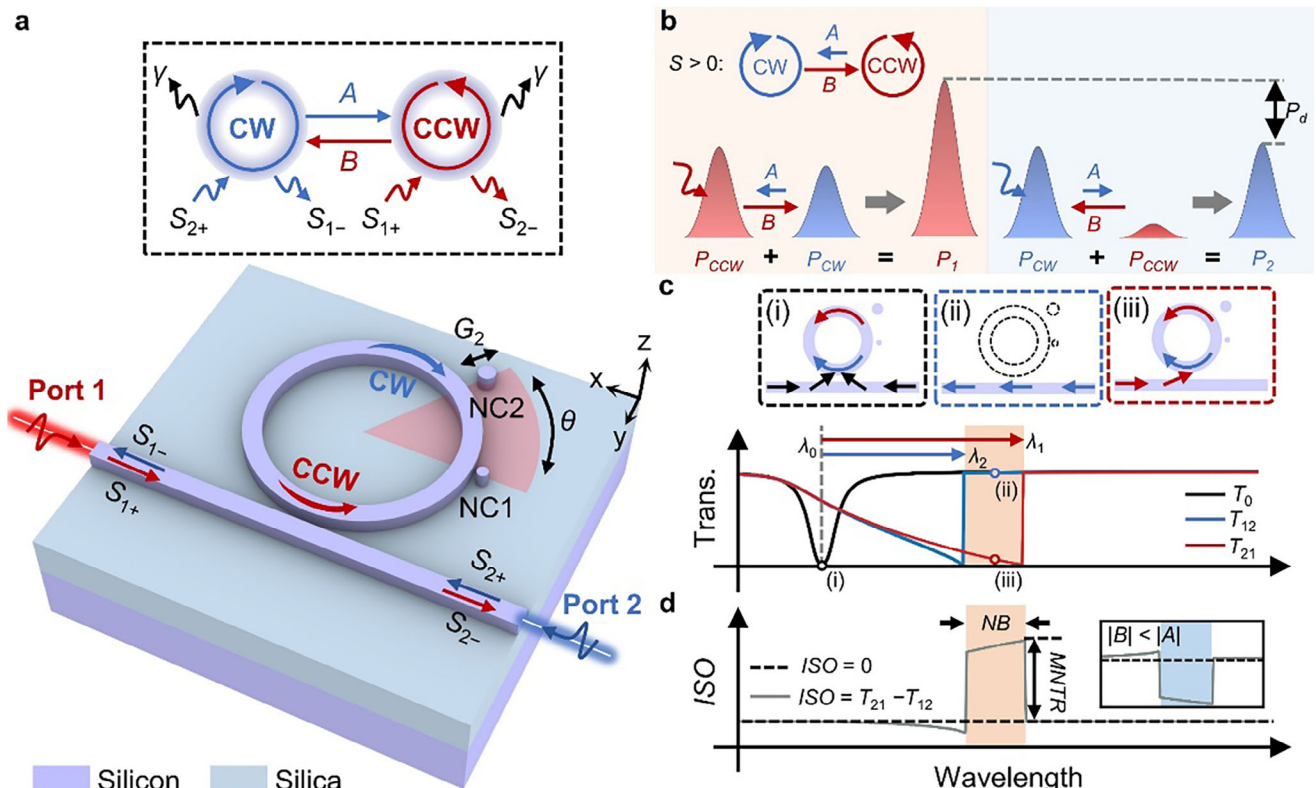


Figure 1. Concept of a chirality-enabled passive photonic diode. a) Schematic of a chiral silicon microring. The chiral silicon microring is composed of an all-pass silicon microring resonator and two nanocylinders (NC1, NC2). The inset shows the corresponding theoretical model. γ represents the loss of the microring resonator. S_{1+} (S_{2+}) represents the amplitude of the incident light from Port 1 (Port 2). The amplitudes of the outgoing wave are expressed as S_{1-} and S_{2-} . b) Intracavity power distribution corresponding to Port 1 (left panel) and Port 2 (right panel) excitations when $S > 0$ ($|B| > |A|$). c) Transmission spectral response in the linear and nonlinear regime when $S > 0$. The black solid curve represents the reciprocal transmission (T_0) spectrum in the linear regime, and λ_0 represents the corresponding resonance wavelength. When the diode operates in the nonlinear regime, the resonance undergoes redshifts. The transmission spectra from excitation at Port 1 ($T_{21} = S_{2-}/S_{1+}$) and Port 2 ($T_{12} = S_{1-}/S_{2+}$) are shown by the solid red and blue curves, respectively. The two resonance dips corresponding to the excitation from Port 1 and 2 are denoted as λ_1 and λ_2 , respectively. The orange-shaded area represents the nonreciprocal band. Insets: schematic describing the flow of light when the diode operates in the linear (i) and nonlinear regime (ii, iii). d) Isolation spectra when the diode operates in the nonlinear regime. The isolation ratio is defined as $ISO = T_{21} - T_{12}$. NB and MNTR represent the nonreciprocal bandwidth and maximum nonreciprocal transmission ratio, respectively. Inset shows the isolation spectrum when $S < 0$ ($|B| < |A|$).

factor and large mode volume in the reported chiral silicon microring.^[35–37]

In this paper, we demonstrate a large bandwidth and low insertion loss passive photonic diode based on a nonlinear chiral microresonator formed by a nanocylinder-loaded silicon microring. The chiral property of the microresonator is triggered and manipulated by perturbing the evanescent field with two nanocylinders. In the nonlinear regime, the microresonator exhibits a direction-dependent intracavity power, resulting in asymmetric wavelength shifts and thus enabling a passive photonic diode. The proposed diode is not constrained by the trade-off between spectral bandwidth and insertion loss. Benefiting from the advantages of a high Q factor and small mode volume, the threshold of the proposed diode can be kept low. Additionally, the diode effect remains valid during the thermal tuning process, which allows the operational bandwidth to be further expanded by incorporating thermal tuning into the microresonator.

2. Results

2.1. Theoretical Model and Design

The proposed photonic diode is constructed using a nanocylinder-loaded silicon microresonator, as shown in Figure 1a (refer to Note S1, Supporting Information for detailed structural parameters). The two nanocylinders are placed close to the outer rim of the microresonator, stimulating asymmetric mutual coupling between clockwise (CW) and counter-clockwise (CCW) modes in the microresonator.^[38] If the coupling from the CW (CCW) mode to the CCW (CW) mode is represented by A (B), the chirality of the system can be quantified as $S = (|B| - |A|)/(|B| + |A|)$.^[33] When $|A| \neq |B|$, the microresonator exhibits a chiral property that can be manipulated by tuning the angular (θ) and radial (G_2) position of the nanocylinders.^[38] When the optical signal incident at the left port (Port 1) of the bus waveguide, the CCW mode is directly excited, while the CW

mode is indirectly excited through asymmetric coupling. When the system is excited from the left port (Port 1), the transmission ($T_{21} = |S_{2-}/S_{1+}|^2$) and reflection ($R_{11} = |S_{1-}/S_{1+}|^2$) can be detected from the right port (Port 2) and Port 1 of the bus waveguide, respectively. Similarly, $T_{12} = |S_{2-}/S_{1+}|^2$ and $R_{22} = |S_{1-}/S_{1+}|^2$ can be detected by exciting the device from Port 2. Due to the chiral property, the intracavity power becomes excitation direction dependent.^[33] Without loss of generality, a chiral microring with $S > 0$ ($|B| > |A|$) is chosen as an example. Figure 1b compares the excitation scenarios from Port 1 (left panel of Figure 1b) and Port 2 (right panel of Figure 1b). As the system supports CW and CCW modes simultaneously, the intracavity power is determined by the combined contributions of the CW and CCW modes. For the convenience of discussion, the intracavity power corresponding to excitation from Port 1 and Port 2 are denoted by P_1 and P_2 , respectively. When the system is excited from Port 2, the coupling from CW mode to CCW mode is suppressed due to destructive interference, resulting in a diminished excitation of the CCW mode. Consequently, a larger portion of power radiates into the space outside the microring, resulting in an increase in overall optical loss. Thus, the intracavity power is lower when the system is excited from Port 2 compared to Port 1 ($P_1 > P_2$). Due to the nonlinear process, the permittivity profile inside the microring is influenced by the intracavity power.^[31–33] Thus, the intracavity power difference ($P_d = P_1 - P_2$) leads to an asymmetric permittivity profile in the nonlinear regime, resulting in asymmetric resonant wavelength drift. Figure 1c shows the spectral responses of a chiral silicon microring in the linear and nonlinear regimes modeled by coupled-mode theory (refer to Note S1, Supporting Information for details).^[39] When the system operates in the linear regime, the transmission spectra in both directions are symmetric, as depicted by the black curve in Figure 1c. A reciprocal Lorentzian lineshaped transmission spectrum centered at the resonant wavelength (λ_0) can be observed as predicted by the Lorentz reciprocity theorem.^[40] Thus, light incident from both Port 1 and Port 2 is coupled from the bus waveguide to the microring resonator at λ_0 (inset i). In the nonlinear regime, the resonant wavelength undergoes redshifts, resulting in a nonlinearity-induced distortion of the resonance lineshapes (refer to Note S1, Supporting Information for a detailed description of the nonlinear process). Due to the intracavity power difference ($P_d > 0$), the resonant wavelength drift for Port 1 excitation is larger than that for Port 2 ($\lambda_1 > \lambda_2$), resulting in the formation of a nonreciprocal band (indicated by the orange-shaded area in Figure 1c). Within the nonreciprocal band, the system exhibits distinct transmission efficiencies for excitations at Port 1 and Port 2. For the Port 2 excitation (inset ii), the incident light that is detuned from resonance propagates through the waveguide with a near-zero insertion loss. In contrast, for excitation from Port 1 excitation (inset iii), the incident light couples into the microring, resulting in prohibited propagation. The asymmetric transmission suggests photonic diode can be realized in the nonlinear chiral microring. Figure 1d shows the isolation spectrum ($ISO = T_{21} - T_{12}$) of the nonlinear chiral microring for $S > 0$ (the inset illustrates the scenario where $S < 0$). The nonreciprocal bandwidth is defined as $NB = \lambda_1 - \lambda_2$.^[33] The maximum nonreciprocal transmission ratio (MNTR) can be observed at the dip of the transmission spectrum for Port 1 excitation.^[17]

The marriage of nonlinearity and chirality diversifies the nonreciprocal properties of the diode, as illustrated in Figure 2. The radii and radial position are set to satisfy the strength condition (refer to Note S1, Supporting Information for the effect of varying radius). The chiral property of the diode can be manipulated by adjusting the angular position of the nanocylinders,^[38] as indicated by the top-left inset of Figure 2a. The proposed photonic diode in this work is engineered for TE polarization. To achieve analogous functionality under TM polarization, the device configuration necessitates systematic optimization guided by the modal field distribution to enable effective chirality manipulation. The spectral response of the diode can be simulated with the dynamical model of nonlinear microring resonators^[41] (refer to Note S1, Supporting Information for details). Figure 2a shows the isolation spectra varying with $\Delta\theta$. When $|B| < |A|$ ($S < 0$), the resonant wavelength for excitation from Port 2 is larger than that from Port 1 ($\lambda_1 < \lambda_2$), resulting in a nonreciprocal band with $ISO < 0$. While $\Delta\theta$ is tuned from negative to positive, the difference between λ_1 and λ_2 diminishes until $\Delta\theta = 0$, where $\lambda_1 = \lambda_2$. At $\Delta\theta = 0$, the CW and CCW modes in the microring are chiral symmetric ($|B| = |A|$), causing the nonreciprocal transmission to vanish ($ISO = 0$). Further increasing $\Delta\theta$ to positive reverses the chiral property of the microring. While $|B| > |A|$ ($S > 0$), $\lambda_1 > \lambda_2$, leading to $ISO > 0$. The transmission spectra from $\Delta\theta < 0$ to $\Delta\theta > 0$ are shown in the top-right inset of Figure 2a (refer to Note S1, Supporting Information for details). The evolution of S and NB is symmetric with respect to $\Delta\theta = 0$, as shown in Figure 2b. As the bus waveguide-microring coupling alters the intracavity power dynamics,^[33] the exceptional points (EP $^\pm$) and the extreme values of nonreciprocal bandwidth (ENB $^\pm$) do not occur at the same $\Delta\theta$. Due to the symmetry of evolutions with respect to $\Delta\theta = 0$, the scenario where $|B| > |A|$ is discussed below for clarity. As shown in the right panel of Figure 2b, the parameter space is divided into two regions, as illustrated by the green- and yellow-shaded areas. In Region I, S increases with $\Delta\theta$. EP $^+$ ($S = +1$) is achieved at the interface between Regions I and II (marked by the yellow dot). With a further increase in $\Delta\theta$ in Region II, the S decreases as NB increases until reaching the extreme (marked by the red dot). It can be observed that diodes with identical S values can exhibit distinct NB . For instance, the diode reaches ENB $^+$ for $\Delta\theta = \Delta\theta_B$. However, when $\Delta\theta = \Delta\theta_A$, the NB of the diode (marked by a green dot) exhibits a discrepancy of over sevenfold compared to $\Delta\theta = \Delta\theta_A$, despite sharing an identical S values (marked by two grey dots). Additionally, the diodes exhibit completely distinct thermal responses in the two regions, as shown in Figure 2c. Figure 2d,e compare the transmission spectra of the diodes in the two regions ($\Delta\theta = \Delta\theta_A$, $\Delta\theta_B$) as ambient temperature increases, which drives the resonant to shift toward longer wavelength due to the thermo-optic effect,^[42] as shown in the inset of Figure 2d. In Region I, the value of NB remains relatively constant, whereas in Region II, a significant change in NB is observed. Consequently, despite the diodes exhibiting identical S values, they demonstrate significantly divergent NB and thermal responses in Regions I and II.

Due to the reliance on optical nonlinearity, the proposed diode displays distinct nonreciprocal properties when excited with different excitation power. Figure 3a shows the transmission response as the P_{in} increases. Initially, the transmission spectra from excitation at Port 1 and Port 2 are reciprocal due to the negligible intracavity power difference. As P_{in} increases, the

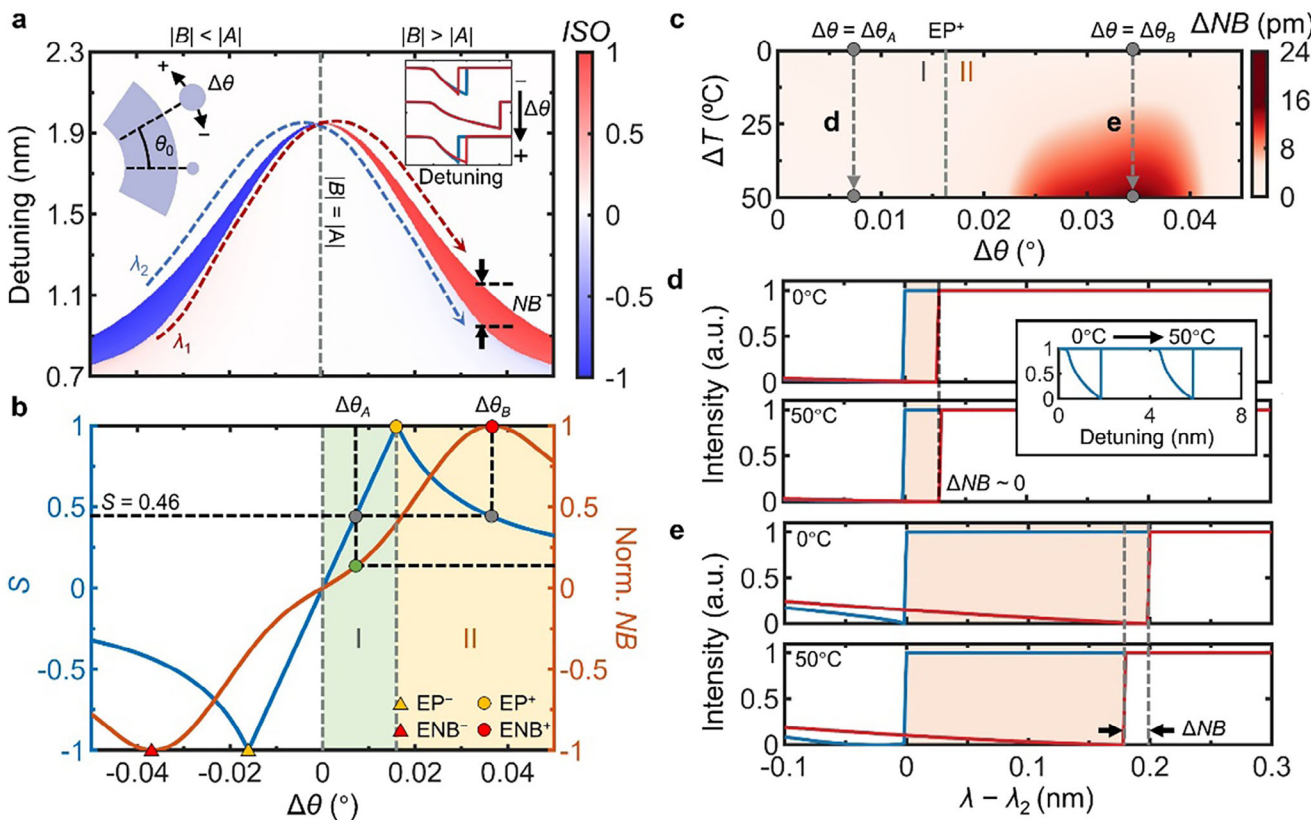


Figure 2. Parametric evolution of the proposed diode. a) Evolution of isolation spectra with $\Delta\theta = \theta - \theta_0$. θ_0 is defined as the angular angle between the two nanocylinders when $S = 0$. The left inset shows the schematic of tuning $\Delta\theta$ by adjusting the angular position of the nanocylinders. The right inset shows the evolution of transmission spectra as $\Delta\theta$ increases. b) Evolution of S (blue curve) and normalized NB (orange curve) with $\Delta\theta$. NB is normalized by the maximum. According to the evolution of S , the parameter space is divided into Region I (green-shaded area) and Region II (yellow-shaded area). The red and yellow triangles represent ENB^- and EP^+ , respectively. The red and yellow dots represent ENB^+ and EP^+ , respectively. When $\Delta\theta = \Delta\theta_A$ and $\Delta\theta = \Delta\theta_B$, the diodes exhibit an identical chiral property ($S = 0.46$), as indicated by the two gray dots. The green dot represents the normalized NB when $\Delta\theta = \Delta\theta_A$. c) Evolution of NB as ambient temperature (ΔT) increases. ΔNB represents the variation of NB with ΔT . $\Delta NB(\Delta\theta) = NB(\Delta\theta, \Delta T = 0) - NB(\Delta\theta, \Delta T)$. d,e) Comparison of the thermal response between the devices in Region I (d) and II (e). The transmission spectrum redshifts in response to an increase in ΔT , as indicated by the inset of (d).

nonlinearity-induced wavelength shift is observed, causing the resonance to transform from a symmetrical Lorentz lineshape to an asymmetric lineshape. As shown in the inset of Figure 3a, the intracavity power difference increases with P_{in} . The threshold of the diode (P_{th}) is defined with $MNTR = 0.5$. The grey-shaded area in Figure 3a represents $P_{in} < P_{th}$, equivalent to $ISO < 3$ dB within the nonreciprocal band. Figure 3b provides zoom-in views of the transmission spectra. When P_{in} is slightly larger than P_{th} (i), the device suffers from a large IL due to the close proximity of λ_1 and λ_2 . Further, increasing P_{in} results in the $MNTR$ approaching unity, while IL decreases toward zero (ii). According to the relationship between P_d and the two coupling coefficients (A, B),^[33] the P_{th} can be tailored by tuning $\Delta\theta$, as shown in Figure 3c. When the diode approaches ENB^+ , the intracavity power difference increases, leading to a reduction in P_{th} . Figure 3d,e compare the transmission characteristic when the diode is steered from non- ENB (Figure 3d) to ENB^+ (Figure 3e). The $MNTR$ and IL varying with P_{in} in the non- ENB state are summarized in the upper panel of Figure 3d. The redshifts of resonant wavelength are shown by the red and blue curves in the lower panel of Figure 3d, respectively. Due to the increasing intracavity power difference, the

magnitude of NB increases with P_{in} , as shown by the black curve in the lower panel of Figure 3d. As depicted in Figure 3d, the proposed diode is not bottlenecked by the trade-off between spectral bandwidth and insertion loss, meaning that large NB and low IL can be realized simultaneously. As shown in Figure 3d, the non-reciprocal properties undergo rapid changes near the threshold power P_{th} . In the vicinity of ENB^+ (Figure 3e), the diode exhibits a low P_{th} , indicating that the diode effect can be achieved with a low P_{in} . Furthermore, owing to the wavelength-dependent perturbations induced by nanocylinders, the proposed diode exhibits distinct nonreciprocal properties across different resonant modes, (refer to Note S1, Supporting Information for details).

2.2. Experimental Result

As shown in Figure 4a, the nanocylinder-loaded microring resonator with $W = 500$ nm, $R = 5 \mu\text{m}$, $r_1 = 40$ nm, $G_1 = 20$ nm, $r_2 = 90$ nm, $G_2 = 50$ nm, and $\theta = 43.16^\circ$ is designed on a 220 nm SOI platform. Such a small microring is deliberately adopted to amplify the interaction between the evanescent field

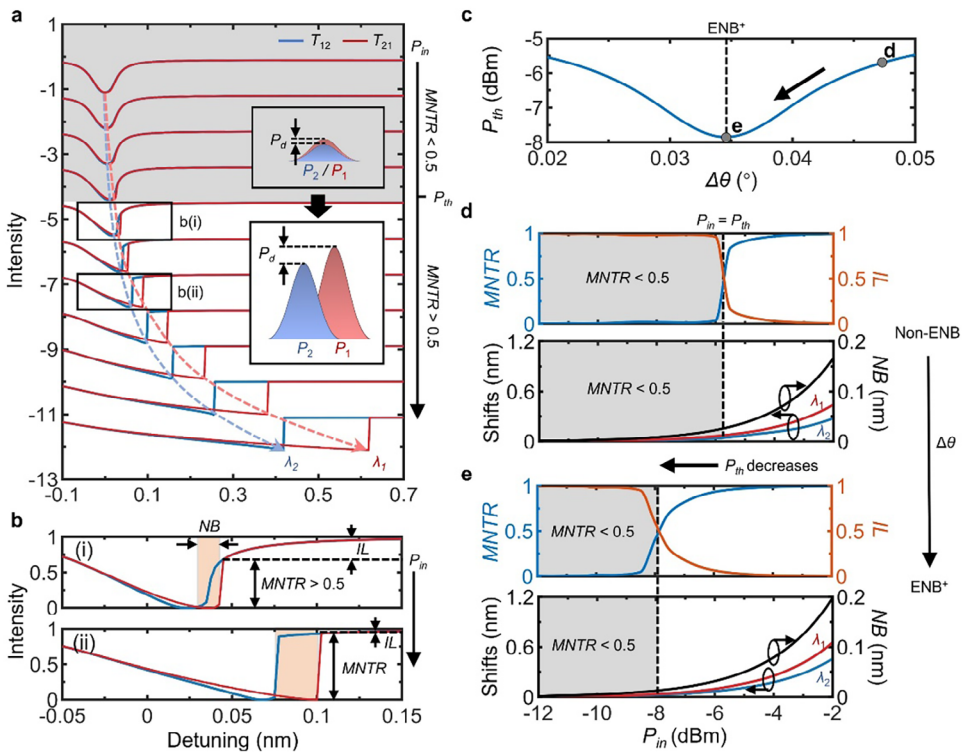


Figure 3. Simulated spectral response of the proposed device as P_{in} increases. a) Simulated transmission spectra as P_{in} increases from top to down. P_{th} is defined as the threshold of the passive photonic diode. Inset shows the schematic of intracavity power corresponding to $P_{in} < P_{th}$ and $P_{in} > P_{th}$. P_d denotes the intracavity power difference. b) Zoomed-in views of the transmission spectra. c) Simulated evolution of P_{th} with $\Delta\theta$. d,e) Transmission characteristics (MNTR, IL, $\Delta\lambda$, and NB) as P_{in} increases. The device is steered from non-ENB⁺ (d) to ENB⁺ (e) by tuning $\Delta\theta$. Two grey dots in (c) represent the two scenarios illustrated in (d and e), respectively.

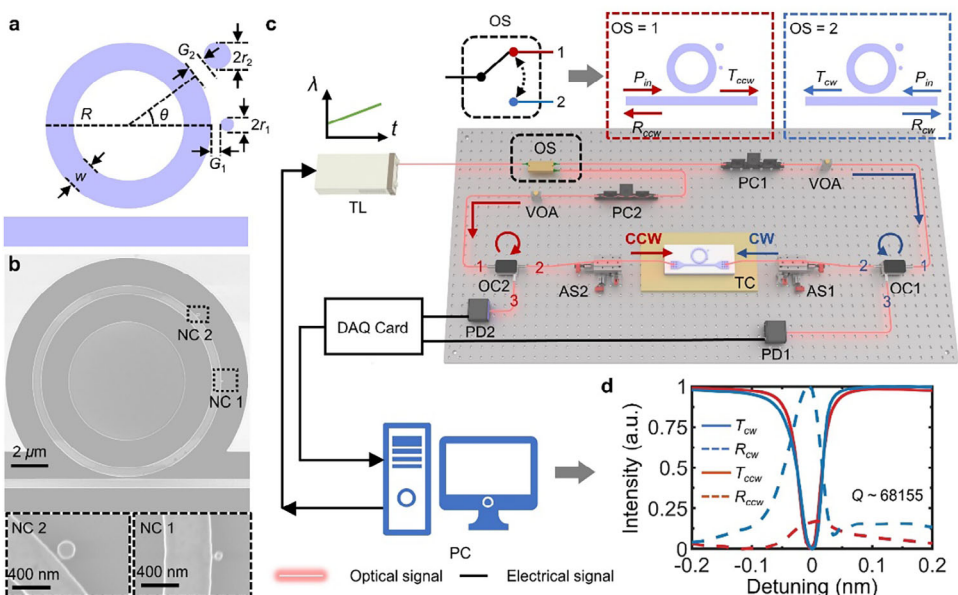


Figure 4. Experimental setup and linear spectral response. a) Schematic of the nanocylinder-loaded microring resonator. b) SEM image of the fabricated sample. c) Schematic of single-side excitation setup. TL: tunable laser; OS: optical switcher; PC: polarization controller; VOA: variable optical attenuator; OC: optical circulator; AS: alignment stage; TC: Temperature controller; PD: photo detector; DAQ: data acquisition; PC: personal computer; d) Linear spectral response of the fabricated devices. The transmission and reflection denoted as T_{cw} and R_{cw} respectively, are excited from the CW direction, while T_{ccw} and R_{ccw} are excited from the CCW direction.

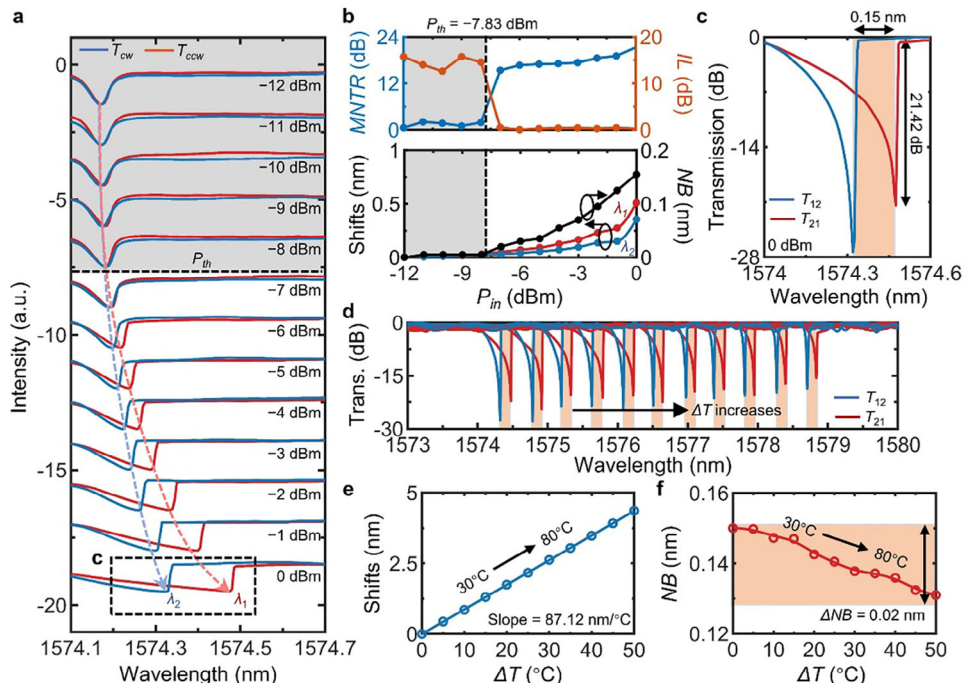


Figure 5. Experimental observation of nonreciprocal properties in the fabricated sample. a) Transmission spectra as P_{in} increases from -12 to 0 dBm. The grey-shaded area represents $P_{in} < P_{th}$. b) Experimental transmission characteristic as P_{in} increases. The orange-shaded area represents the nonreciprocal band. c) Zoom-in view of the transmission spectra at $P_{in} = 0$ dBm. d) Experimental transmission spectra as the ΔT increases. The p_{in} is set to 0 dBm. e,f) Wavelength shifts (λ_1) and evolution of NB corresponding to (d).

and the nanocylinders, thereby enabling the introduced perturbation to effectively modulate the intracavity power distribution. The size and geometry of the nanocylinders were strategically selected to achieve fabrication-tolerant chirality manipulation, thereby mitigating fabrication constraints in the realization of photonic diodes (refer to Note S1, Supporting Information for details). The gap between the bus waveguide and microring is optimized to satisfy the critical coupling condition. Subwavelength grating couplers^[43] are used for fiber-to-chip coupling. In this work, we focus on the on-chip insertion loss. Therefore, the losses associated with fiber-to-chip coupling, such as those induced by grating couplers, polarization controllers (PCs), and variable optical attenuators (VOAs), are excluded from the analysis. The sample is fabricated using electron beam lithography and inductively coupled plasma etching (refer to Fabrication and Note S2, Supporting Information for details). Figure 4b shows the scanning electron microscopy (SEM) images of the fabricated sample. The zoom-in views of the two nanocylinders are shown in the inset of Figure 4b. As shown in Figure 4c, a single-side excitation setup is used to measure the spectral response (refer to subhead “Characterization” in Experimental Section and Note S2, Supporting Information for details). To investigate the nonreciprocal properties of the sample, the device is sequentially excited from CW and CCW directions, which is controlled by the optical switch (OS). When OS = 1, the device is excited in the CCW direction, whereas when OS = 2, the device is excited in the CW direction. To investigate the linear behavior of the fabricated sample, the spectral response is measured under the excitation power with -18 dBm. A chiral resonance with a Q factor

of ≈ 68155 is observed. As shown in Figure 4d, the transmission spectra are reciprocal, while the reflection spectra are asymmetric. The asymmetric reflection spectra evidence that the coupling from the CCW direction to the CW direction is suppressed.^[38] Based on the reflection peaks from two directions, the chirality S of the fabricated device is estimated to be ≈ 0.41 .^[44] Since the measured S is slightly less than S_{ENB+} , the fabricated sample is in the vicinity of ENB⁺.

Figure 5a shows the transmission response as P_{in} increases from -12 to 0 dBm (refer to Note S2, Supporting Information for the corresponding isolation spectra). When $P_{in} = -12$ dBm, the transmission spectra remain nearly reciprocal, which precisely matches the theoretical prediction. As P_{in} increases, the transmission spectra become asymmetric, resulting in the formation of a nonreciprocal band. The intracavity powers (P_1 , P_2) increase with P_{in} , resulting in the redshifts of the resonances (λ_1 , λ_2) as indicated by the red and blue dashed lines in Figure 5a. λ_1 shifts from 1574.175 to 1574.475 nm, meanwhile, λ_2 shifts from 1574.17 to 1574.32 nm. Due to $S > 0$, NB increases with P_{in} . The NB and $MNTR$ are summarized in Figure 5b. When P_{in} exceeds -8 dBm, the $MNTR$ experiences a rapid increase, suggesting that P_{in} is in close proximity to P_{th} , which is estimated to be -7.83 dBm. For $P_{in} > P_{th}$, NB increases with P_{in} , while $MNTR$ also increases, which is consistent with the prediction in Figure 4. Figure 5c shows the transmission spectra at $P_{in} = 0$ dBm, where a passive photonic diode with $NB \approx 0.15$ nm (18.75 GHz) and $MNTR \approx 21.42$ dB is observed. The $MNTR$ can be further enhanced through precise adjustment of the gap between the bus waveguide and the microring.^[33] To investigate the thermal re-

sponse of the proposed diode, the transmission spectra are measured as the ambient temperature increases from 30 to 80 °C. As shown in Figure 5d, the resonances undergo redshifts due to the thermal-optical effect. The λ_1 and NB varying with ΔT are summarized in Figure 5e. The slope of λ_1 is estimated to be 87.12 pm °C⁻¹. The NB decreases as the temperature increases. As shown in Figure 5f, a maximum variation of 0.02 nm (2.38 GHz) is observed when ΔT is tuned from 30 to 80 °C. According to the thermal response, the fabricated sample is in Region II shown in Figure 2c. Assisted by thermal tuning with $\Delta T = 50$ °C, the bandwidth of the diode can reach 4.52 nm with an IL of 0.46 dB.

3. Discussion

By reducing P_{th} , the chirality-enabled diode can overcome the constraints of high excitation power requirements typically associated with nonlinear devices. One effective strategy involves increasing the P_d while maintaining a constant P_{in} . By increasing the Q value and reducing the mode volume, it is possible to effectively increase P_d in chiral microresonators, thereby achieving a low P_{th} . For the reported chiral silicon microrings,^[35–37] the limited Q factor (e.g., 2.1×10^4) and large mode volume (e.g., 5.0×10^{-17} m³) resulted in a high P_{th} , which prohibited the construction of a low P_{th} photonic diode. In contrast, benefiting from the low additional loss induced by two nanocylinders, the proposed diode exhibits the advantages in a high Q factor ($\approx 6.8 \times 10^4$) and small mode volume ($\approx 5.9 \times 10^{-18}$ m³). Consequently, the proposed microring resonator demonstrates superior capability in achieving a lower P_{th} (refer to Note S1, Supporting Information for details). In addition, analogous chiral manipulation may be achieved through the incorporation of multiple nanoscatteers within the evanescent field of the resonant mode (refer to Note S1, Supporting Information for details). In contrast to the dual-nanocylinder configuration, however, the multi-scatterer configuration introduces elevated intracavity losses, which significantly raise the operational threshold. Upon comparing the experimental results (Figure 5) with the simulation (Figure 3), it is observed that the fabricated sample exhibits a slight deviation from the ENB⁺ due to fabrication constraints and sidewall roughness. Implementing external control mechanisms (e.g., localized thermo-optic tuning)^[29] to precisely regulate $\Delta\theta$ can further minimize P_{th} . Additionally, enhancing the nonlinear effects of the proposed diode may facilitate a further reduction in P_{th} . For instance, introducing the mechanical Kerr effect^[17] can yield a stronger nonlinear response. Improving the thermal properties of the proposed diode—such as employing silicon substrate undercut to accumulate in the vicinity of the waveguide^[45]—may also contribute to a further decrease in P_{th} . The temporal response of thermal nonlinearity-enabled photonic diodes is intrinsically bounded to the microsecond regime due to thermal dissipation.^[13] However, this inherent latency proves advantageous for one-way transmission of high-speed modulated data streams, as extended integration intervals mitigate sensitivity to transient fluctuations arising from rapid data pattern variations or diverse modulation schemes.^[12] Additionally, through optimization of the thermal environment and excitation power, the response time of thermal nonlinearity-based photonic diodes can be reduced to sub-microsecond levels,^[15] enabling deployment in pulsed applications such as pulse routing in LiDAR systems.^[8]

4. Conclusion

In conclusion, we propose a chirality-based passive photonic diode in SOI platform with $NB \approx 18.75$ GHz, $IL \approx 0.46$ dB, and $MNTR \approx 21.42$ dB under 0 dBm excitation power. The P_{th} is estimated to be -7.83 dBm. In addition, the thermal tunability of the working wavelength is verified. The proposed device exhibits significant advantages in spectral bandwidth, insertion loss, and tunability (see the comparison table in Note S3, Supporting Information). Our study paves the way for the large-scale integration of passive photonic diodes in silicon photonic platforms.

5. Experimental Section

Fabrication: The samples were fabricated on the typical SOI platform with a 220-nm-thick single-crystal silicon layer and a 2-μm buried oxide layer. First, diluted positive electron beam resist (ZEP520A) was spinning coated on a piranha-cleaned SOI chip and baked at 180 °C for 5 min. Then, the pattern was transferred to the resist film by electron beam lithography (Elionix ELS-F125G8) with a dose of 220 μC cm⁻² and an accelerating voltage of 125 kV. The exposed resist was developed in amylacetate for 100s and rinsed in isopropanol for 30s. To transfer the pattern from the resist film to the silicon layer, ICP reactive-ion etching was used with a gas mixture of CHF₃ and SF₆ for 130s. Finally, the residual resist was removed by dimethyl sulfoxide.

Characterization: To investigate the nonreciprocal properties of the fabricated sample, the transmission and reflection spectra for excitation from CW or CCW direction were monitored. A single-side excitation setup was employed as shown in Figure 4c. The fabricated sample was mounted on a temperature controller (TC) to meticulously regulate its temperature. A tunable laser (Santec TLS-550) with a 5 pm wavelength step size was used as the source. The wavelength sweeps from blue to red. The input direction (CW or CCW direction) was selected by an optical switch (OS). The polarization of the incident light was controlled by the fiber polarization controller (PC1, PC2). Two variable optical attenuators (VOAs) were employed to ensure symmetrical optical power input into the chip from both directions. Two grating couplers were employed for fiber-to-chip coupling. To minimize the impact of reflection within the measurement setup, the fibers utilized for interfacing the chip and light source were polished at an angle of 8°. Two alignment stages (AS1, AS2) were employed to optimize the efficiency of fiber-to-chip coupling. Transmission and reflection spectra at port 3 of the two circulators (OC1, OC2) were monitored by the photodiodes (PD1, PD2). The signal was acquired by a DAQ card and analyzed by a PC.

Supporting Information

Supporting Information is available from the Wiley Online Library or from the author.

Acknowledgements

This research was supported by the National Natural Science Foundation of China (NSFC) (U22A2093); Science, Technology and Innovation Commission of Shenzhen Municipality (JCYJ20210324131614040; GXWD20231130113557001); Basic and Applied Basic Research Foundation of Guangdong Province (2020B1515130006; 2021B1515120056).

Conflict of Interest

The authors declare no conflict of interest.

Data Availability Statement

The data that support the findings of this study are available in the supplementary material of this article.

Keywords

low-threshold, nonlinear chiral microrings, nonreciprocal transmission, silicon photonic diodes

Received: December 2, 2024

Revised: April 10, 2025

Published online: June 7, 2025

- [1] V. S. Asadchy, M. S. Mirmoosa, A. Díaz-Rubio, S. Fan, S. A. Tretyakov, *Phys. Rev. Appl.* **2018**, *10*, 047001.
- [2] V. S. Asadchy, M. S. Mirmoosa, A. Díaz-Rubio, S. Fan, S. A. Tretyakov, *Proc. IEEE* **2020**, *108*, 1684.
- [3] M. Cotrufo, S. A. Mann, H. Moussa, A. Alu, *IEEE Trans. Microwave Theory Tech.* **2021**, *69*, 3569.
- [4] D. L. Sounas, A. Alù, *Nat. Photonics* **2017**, *11*, 774.
- [5] M. Cotrufo, S. A. Mann, H. Moussa, A. Alu, *IEEE Trans. Microwave Theory Tech.* **2021**, *69*, 3584.
- [6] J. Qin, S. Xia, W. Yang, H. Wang, W. Yan, Y. Yang, Z. Wei, W. Liu, Y. Luo, L. Deng, L. Bi, *Nanophotonics* **2022**, *11*, 2639.
- [7] W. Yan, Y. Yang, W. Yang, J. Qin, L. Deng, L. Bi, *IEEE J. Sel. Top. Quantum Electron.* **2022**, *28*, 6100515.
- [8] K. Y. Yang, J. Skarda, M. Cotrufo, A. Dutt, G. H. Ahn, M. Sawaby, D. Vercruyse, A. Arbabian, S. H. Fan, A. Alù, J. Vuckovic, *Nat. Photonics* **2020**, *14*, 369.
- [9] L. Bi, J. Hu, P. Jiang, D. H. Kim, G. F. Dionne, L. C. Kimerling, C. A. Ross, *Nat. Photonics* **2011**, *5*, 758.
- [10] Z. Shen, Y.-L. Zhang, Y. Chen, C.-L. Zou, Y.-F. Xiao, X.-B. Zou, F.-W. Sun, G.-C. Guo, C.-H. Dong, *Nat. Photonics* **2016**, *10*, 657.
- [11] D. L. Sounas, A. Alù, *IEEE Antennas Wirel. Propag. Lett.* **2018**, *17*, 1958.
- [12] J. Wang, L. T. Varghese, L. Fan, P.-H. Wang, Y. Xuan, D. E. Leaird, A. M. Weiner, M. Qi, *Opt. Express* **2014**, *22*, 25739.
- [13] A. Li, W. Bogaerts, *Optica* **2020**, *7*, 7.
- [14] M. Cotrufo, A. Cordaro, D. L. Sounas, A. Polman, A. Alù, *Nat. Photonics* **2023**, *18*, 81.
- [15] L. Fan, J. Wang, L. T. Varghese, H. Shen, B. Niu, Y. Xuan, A. M. Weiner, M. Qi, *Science* **2012**, *335*, 447.
- [16] L. Fan, L. T. Varghese, J. Wang, Y. Xuan, A. M. Weiner, M. Qi, *Opt. Lett.* **2013**, *38*, 1259.
- [17] L. Ren, X. Xu, S. Zhu, L. Shi, X. Zhang, *ACS Photonics* **2020**, *7*, 2995.
- [18] Y. Yu, Y. Chen, H. Hu, W. Xue, K. Yvind, J. Mork, *Laser Photon. Rev.* **2015**, *9*, 241.
- [19] M. Xu, J. Wu, T. Wang, X. Hu, X. Jiang, Y. Su, *IEEE Photon. J.* **2013**, *5*, 2200307.
- [20] Y. Shi, Z. Yu, S. Fan, *Nat. Photonics* **2015**, *9*, 388.
- [21] L. Del Bino, J. M. Silver, M. T. M. Woodley, S. L. Stebbings, X. Zhao, P. Del'Haye, *Optica* **2018**, *5*, 279.
- [22] A. Li, H. Wei, M. Cotrufo, W. Chen, S. Mann, X. Ni, B. Xu, J. Chen, J. Wang, S. Fan, C. W. Qiu, A. Alu, L. Chen, *Nat. Nanotechnol.* **2023**, *18*, 706.
- [23] H. Cao, J. Wiersig, *Rev. Mod. Phys.* **2015**, *87*, 61.
- [24] C. Wang, Z. Fu, W. Mao, J. Qie, A. D. Stone, L. Yang, *Adv. Opt. Photonics* **2023**, *15*, 442.
- [25] M. Kim, K. Kwon, J. Shim, Y. Jung, K. Yu, *Opt. Lett.* **2014**, *39*, 2423.
- [26] J. Li, M. Tang, J. Duan, X. Xu, K. Xu, L. Ma, J. Wang, *J. Lightwave Technol.* **2023**, *41*, 2870.
- [27] W. Chen, S. K. Ozdemir, G. Zhao, J. Wiersig, L. Yang, *Nature* **2017**, *548*, 192.
- [28] C. Wang, X. Jiang, G. Zhao, M. Zhang, C. W. Hsu, B. Peng, A. D. Stone, L. Jiang, L. Yang, *Nat. Phys.* **2020**, *16*, 334.
- [29] Y. Chen, J. Li, K. Xu, S. Biasi, R. Franchi, C. Huang, J. Duan, X. Wang, L. Pavesi, X. Xu, J. Wang, *Laser Photon. Rev.* **2024**, *18*, 2301289.
- [30] C. Wang, W. R. Sweeney, A. D. Stone, L. Yang, *Science* **2021**, *373*, 1261.
- [31] R. Franchi, S. Biasi, A. M. de las Heras, M. Ghulinyan, I. Carusotto, L. Pavesi, *Opt. Express* **2021**, *29*, 29615.
- [32] A. M. de las Heras, R. Franchi, S. Biasi, M. Ghulinyan, L. Pavesi, I. Carusotto, *Phys. Rev. Appl.* **2021**, *15*, 054044.
- [33] J. Qie, C. Wang, L. Yang, *Laser Photon. Rev.* **2023**, *17*, 2200717.
- [34] L. Ren, S. Yuan, S. Zhu, L. Shi, X. Zhang, *ACS Photonics* **2023**, *10*, 3797.
- [35] S. Biasi, R. Franchi, F. Mione, L. Pavesi, *Photonics Res.* **2022**, *10*, 1134.
- [36] R. Franchi, S. Biasi, D. Piciocchi, L. Pavesi, *APL Photonics* **2023**, *8*, 056111.
- [37] H. Lee, A. Kecebas, F. Wang, L. Chang, S. K. Özdemir, T. Gu, *eLight* **2023**, *3*, 20.
- [38] J. Li, W. Li, Y. Feng, J. Wang, Y. Yao, Y. Sun, Y. Zou, J. Wang, F. He, J. Duan, G. J. Chen, P. P. Shum, X. Xu, *Nano Lett.* **2024**, *24*, 3906.
- [39] W. Suh, Z. Wang, S. Fan, *IEEE J. Quantum Electron.* **2004**, *40*, 1511.
- [40] A. Calabrese, F. Ramiro-Manzano, H. M. Price, S. Biasi, M. Bernard, M. Ghulinyan, I. Carusotto, L. Pavesi, *Photonics Res.* **2020**, *8*, 1333.
- [41] T. J. Johnson, M. Borselli, O. Painter, *Opt. Express* **2006**, *14*, 817.
- [42] S. Liu, J. Feng, Y. Tian, H. Zhao, L. Jin, B. Ouyang, J. Zhu, J. Guo, *Front. Optoelectron.* **2022**, *15*, 9.
- [43] X. Xu, H. Subbaraman, J. Covey, D. Kwong, A. Hosseini, R. T. Chen, *Appl. Phys. Lett.* **2012**, *101*, 031109.
- [44] B. Peng, S. K. Ozdemir, M. Lierter, W. Chen, J. Kramer, H. Yilmaz, J. Wiersig, S. Rotter, L. Yang, *Proc. Natl. Acad. Sci. U.S.A.* **2016**, *113*, 6845.
- [45] N. C. Harris, Y. Ma, J. Mower, T. Baehr-Jones, D. Englund, M. Hochberg, C. Galland, *Opt. Express* **2014**, *22*, 10487.